The Astrophysical Journal, 590:906–916, 2003 June 20

THE IMPACT OF IONIZING STARS ON THE DIFFUSE INTERSTELLAR MEDIUM: A SWEPT-UP SHELL AND IONIZED HALO AROUND THE W4 CHIMNEY/SUPERBUBBLE

S. Terebey,[1,2] M. Fich,[3] R. Taylor,[4] Y. Cao,[5] and T. Hancock[2]

Received 2001 August 7; accepted 2003 March 5

ABSTRACT

Normandeau et al. have suggested that W4 is a Galactic chimney powered by the OCl 352 cluster, and subsequent work adds to its status as the prime candidate chimney in our Galaxy. The model proposes that the massive star cluster OCl 352 powers a superbubble that achieved "blowout" to form a Galactic chimney. In this picture blowout occurs above the Galactic plane because of a density gradient in the interstellar medium. Using the $\sim 1'$ resolution far-infrared *IRAS* IGA and radio DRAO CGPS Galactic plane surveys, we analyze the neutral and ionized components of the W4 chimney/superbubble. We show that W4 has a swept-up, partially ionized shell of gas and dust that is powered by the OCl 352 star cluster. Dust optical depth maps show dense interstellar material below the shell and provide direct evidence of the dense gas that caused the lower shell expansion to stall. Although parts of the shell are found to be ionization-bounded, the shell is very inhomogenous, and an ionized halo provides evidence of significant Lyman continuum leakage. A large fraction (40%) of the OCl 352 cluster photons escape to large distances and are available to ionize the Galactic halo and the diffuse ionized gas component of the interstellar medium.

Subject headings: Galaxy: structure — H II regions — infrared: ISM — ISM: bubbles — ISM: individual (W4 Superbubble) — ISM: structure

1. INTRODUCTION

There is increasing evidence that massive star clusters play a large role in ionizing the diffuse interstellar gas (DIG), or warm ionized medium (WIM). In addition to their ionizing radiation, OB clusters inject energy into the interstellar medium (ISM) through stellar winds or supernovae to form large dynamical structures, such as wind-blown bubbles and galactic chimneys. Theoretical arguments suggest that galactic chimneys may be an important conduit to galactic halos, by providing ionizing photons or supplying hot gas (Mac Low, McCray, & Norman 1989; Dove & Shull 1994; Shull 1996). There is theoretical debate about whether chimneys form via superbubble blowout (Cox 1989; Tomisaka 1998). However, the data presented here are not directly sensitive to hot gas, and for our purpose the term chimney is used to mean a low-density channel through which ionizing photons can travel.

The diffuse ionized gas in our Galaxy lies in a thick and fairly pervasive layer with filling factor $f > 0.2$, scale height of ~ 1 kpc, and electron number density $n_e \sim 0.08$ cm^{-3} (Reynolds 1991; Kulkarni & Heiles 1987). Reynolds (1984) has argued that only OB stars can satisfy the ionization power requirements, a result supported by theoretical models of DIG and Galactic halo ionization (Miller & Cox 1993; Dove & Shull 1994). Persuasive evidence that Lyman continuum photons can escape local H II region environs to travel large distances is provided by studies of external galaxies, which show that the DIG is highly correlated with bright H II regions over both small and large scales and comprises a high fraction, up to 50%, of the total Hα flux (Walterbos & Braun 1994; Ferguson et al. 1996; Oey & Kennicutt 1997). However, counterevidence against this interpretation comes from He recombination line observations, which suggest that the interstellar radiation field is softer than would be expected from H II region models (Reynolds & Tufte 1995; Reynolds, Haffner, & Tufte 1999).

Theoretical models of DIG and halo ionization by O stars by necessity modify the traditional view of H II regions as ionization-bounded entities defined by a Strömgren radius. However, the models, as yet, incorporate a simplified ISM structure compared with the highly inhomogeneous nature of the ISM (Miller & Cox 1993; Dove & Shull 1994). Observational studies of H II regions, such as this investigation of W4, provide a direct method to assess the relative importance of ISM components, such as clouds, bubbles, and chimneys, to the transport of ionizing flux.

This paper presents a detailed analysis of the radio and far-infrared (FIR) emission from the W4 H II region, the prime candidate chimney in the Milky Way. On the basis of a large H I void, Normandeau, Taylor, & Dewdney (1996) have proposed that W4 is a Galactic chimney powered by the OCl 352 (IC 1805/Cas OB 6) massive star cluster. Basu, Johnstone, & Martin (1999) model the chimney as a wind-blown superbubble. Recent H II results (Reynolds, Sterling, & Haffner 2001) suggest a kiloparsec-sized void that extends much higher above the Galactic plane than that derived from the original H I result. In many respects, the W4 giant H II region and OCl 352 massive star cluster have fairly typical properties, so that the results derived for W4 may be applicable to the larger question of how the DIG and gaseous halos in galaxies are fueled and ionized. The ambient density near W4 of 5 cm^{-3} (Normandeau et al. 1996) is similar to that of the LMC, which is known to contain a large number of wind-blown bubbles (Braunsfurth & Feitzinger 1983).

[1] Department of Physics and Astronomy, California State University, 5151 State University Drive, Los Angeles, CA 90032-8206.
[2] Extrasolar Research Corporation, 2026 Hall Canyon Drive, La Cañada, CA 91011.
[3] Department of Physics, University of Waterloo, Waterloo, ON, Canada.
[4] Department of Physics and Astronomy, University of Calgary, Calgary, AB, Canada.
[5] KLA Tencor Corporation, San Jose, CA.

In this paper, we find that most of the star cluster's ionizing photons escape the W4 superbubble/chimney and are therefore available to ionize the ISM at large distances. This result disagrees with Hα results, which, however, are affected by uncertainties in the extinction correction (Dennison, Topasna, & Simonetti 1997). In addition, we find that the W4 superbubble displays ionization-bounded characteristics. Roughly 20% of the ionizing photons are trapped in an inhomogeneous thin shell below the massive star cluster. The FIR and radio data show that some parts of the shell are thick enough to trap the ionizing photons, and they further show that the shell's inner edge is lined by ionized gas and heated dust. However, the shell is patchy, so that a faint halo of ionized gas and heated dust extends beyond the shell's boundary.

1.1. *Overview of the W3-W4-W5 Region*

To study W4 we use data from several recent Galactic plane surveys. The *IRAS* Galaxy Atlas (IGA) provides high spatial resolution, processed *IRAS* images of the Galactic plane at FIR wavelengths (Cao et al. 1997). The IGA, in conjunction with the DRAO H I line/21 cm continuum (Normandeau, Taylor, & Dewdney 1997) and FCRAO CO (1–0) line (Heyer et al. 1998) Galactic plane surveys, both with similar ($\sim 1'$) resolution, provides a powerful venue for studying the ISM and large-scale structure in our Galaxy.

Figure 1 shows a panoramic view encompassing the W3, W4, and W5 H II regions located in the Perseus spiral arm in the outer Galaxy (Heyer & Terebey 1998). In the infrared, W4 and W5 display pronounced loop structure, suggestive of wind-swept shells powered by OB clusters, while W3's compact size indicates a young H II region that is related to star formation activity in the W3 molecular cloud. A CO-IR survey shows many sites of active star formation (Carpenter, Heyer, & Snell 2000). Comparison of the 60 μm emission (*left-hand panel*) with the 21 cm continuum emission (*right-hand panel*) illustrates the close correspondence of the FIR to radio continuum emission. Previous studies show that the ratio of FIR to 2.7 GHz radio continuum flux density is high for H II regions ($\sim$1000) as compared with supernova remnants ($<$10; Fürst, Reich, & Sofue 1987; Haslam & Osborne 1987). Based on this discriminator between thermal and nonthermal regions, after an approximate correction for the different radio frequency, most of the structure in Figure 1 appears due to thermal emission. In § 3.3, we apply a stronger test and find that the spectral index of 0.08 derived for the W4 loop is consistent with free-free, rather than nonthermal, emission.

At a distance of 2.2 kpc, the W4 H II region provides a striking example of dynamically formed features in the ISM. Normandeau et al. (1996) propose that W4 is a superbubble, powered by the OCl 352 (IC 1805) OB cluster ($l = 135°$, $b = 1°$), that has achieved blowout to form a Galactic chimney. The evidence for a chimney includes a large, "cone-shaped" void in the H I gas directly above the OCl 352 cluster (Normandeau et al. 1996; indicated schematically in Fig. 1), as well as an accompanying faint Hα shell that extends 6° above the stellar cluster (Dennison et al. 1997). The H I data (Normandeau et al. 1996) indicate that the neutral ISM exhibits the lowest density above the OCl 352 cluster (the chimney region) and has the highest density below the star cluster (the loop region). Located directly below the OCl 352 cluster and prominent in both Figures 1 and 2 is the W4 loop ($\sim 1° \sim 40$ pc), visible in infrared, radio continuum, and Hα emission. The W4 loop is interpreted as the lower half of the W4 superbubble, its smaller size (as compared with the chimney) presumed to indicate "stalled" expansion into higher ambient density material. Basu et al. (1999) further support this physical picture, modeling the W4 region as a wind-blown bubble expanding into a vertically stratified medium that has a steep density gradient. The radio continuum data show a

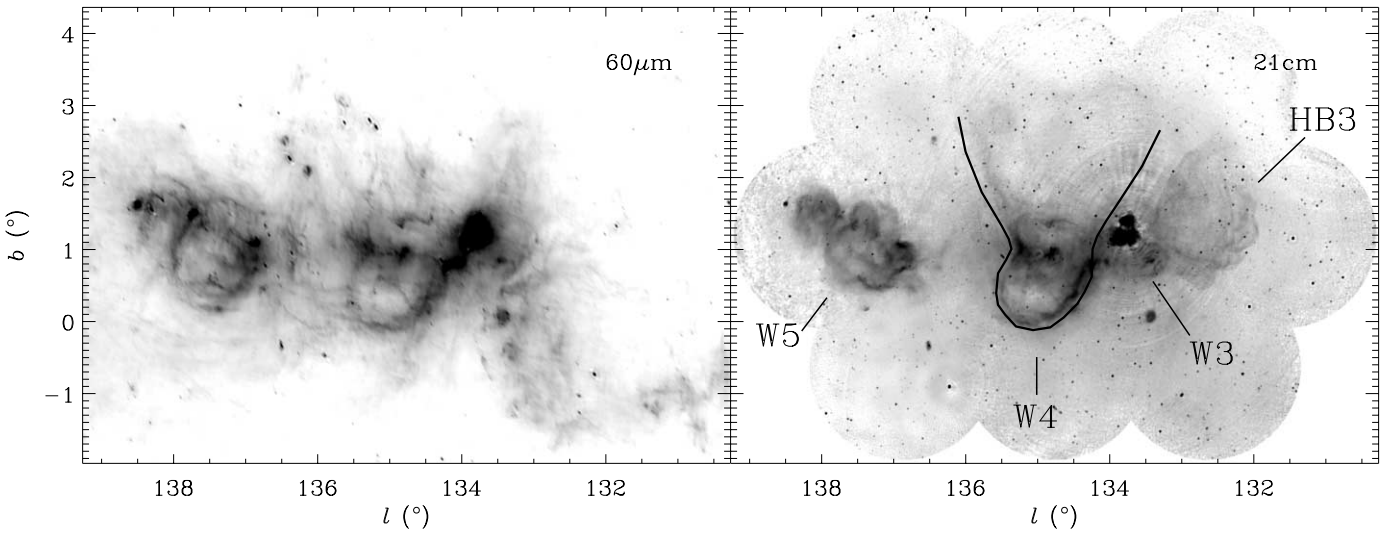

FIG. 1.—Panoramic FIR and radio images of the W3-W4-W5 outer Galaxy H II regions. The strong correspondence between the infrared and radio continuum emission toward the H II regions demonstrates a tight coupling between warm dust (60 and 100 μm) and ionized gas (21 cm). An inverse color table is used, so bright = black. *Left*: *IRAS* 60 μm data; data for 100 μm look nearly identical. Note that both W4 and W5 exhibit loop structure, suggestive of limb-brightened shells. Display uses 1.0 MJy sr^{-1} $<$ log I_{60} $<$ 2.5 MJy sr^{-1}. *Right*: The 21 cm continuum emission; 73 cm continuum looks nearly identical. The W3, W4, and W5 H II regions and HB 3 supernova remnant are identified. W3 is a region of active star formation. The solid line shows the approximate outline of the proposed W4 Galactic chimney; this model invokes an ambient density gradient to explain blowout to the top (Normandeau et al. 1996). The display uses 0 K $<$ log I_{21} $<$ 1.2 K, in brightness temperature units.

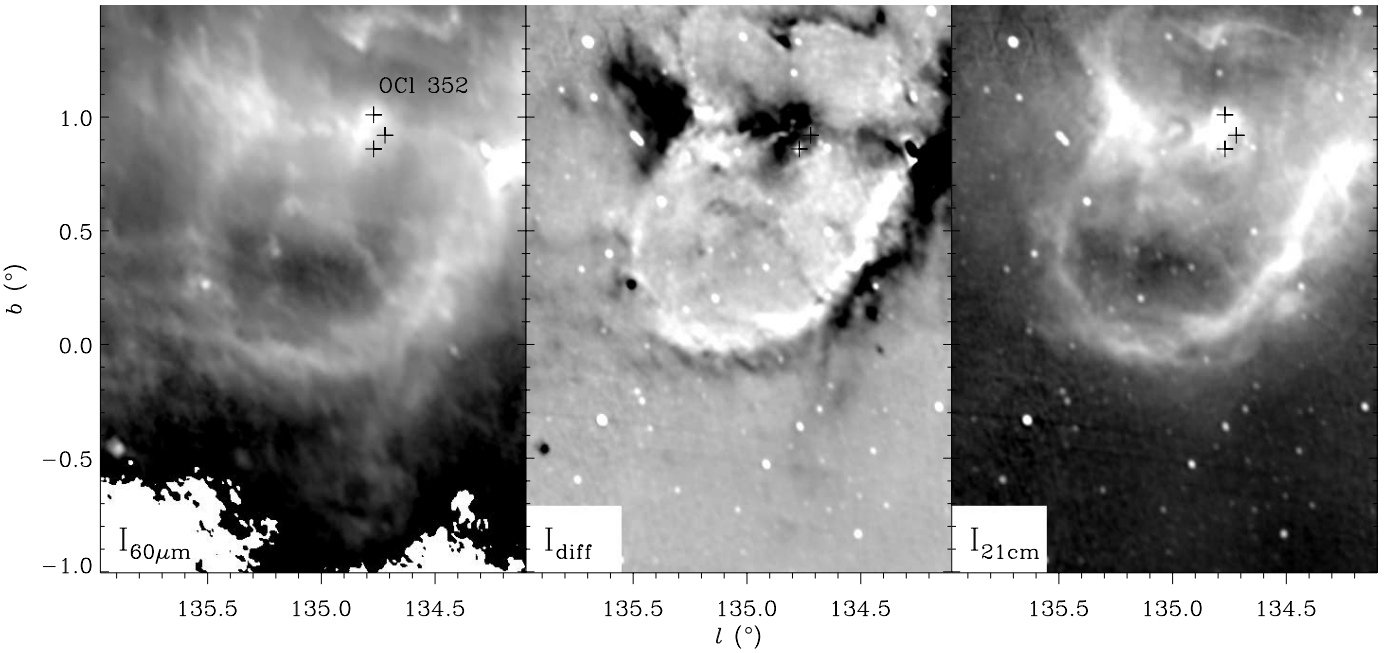

FIG. 2.—Close-up of the W4 loop region, showing striking spatial differences between the infrared and radio continuum emission. Difference images show that ionized gas (*white*) lies interior to warm dust (*black*) across the shell. Positions of the three earliest O stars in the OCl 352 OB cluster are marked. A default color table is used, so bright = white. *Left*: 60 μm data. The display uses 0.5 Jy arcmin^{-2} < log I_{60} < 2.5 Jy arcmin^{-2}. *Right*: 21 cm continuum data; −2.1 Jy arcmin^{-2} < log I_{21} < −1.2 Jy arcmin^{-2}. *Middle*: Difference image, as described in text. The display uses $-0.02 < I_{\rm diff} < 0.015$.

low-density halo surrounding the W4 loop (Gray et al. 1999).

The stellar properties of the OCl 352 cluster show that it is a fairly typical optical OB association, containing nine O stars and 4.3×10^6 $L_\odot$ luminosity (Massey, Johnson, & DeGioia-Eastwood 1995; Normandeau et al. 1996). A trio of massive stars (O4–O5) provide most of the ionizing radiation. The FIR and radio emission are not symmetric around the cluster; Figure 1 shows that little emission lies above the cluster position, except for a dense cometary-shaped cloud, which is being photoionized and eroded by the OB cluster (Heyer et al. 1996; Taylor et al. 1999). This further suggests that the region above the cluster (chimney) has much lower density, on average, than is found below the star cluster in the W4 loop region (Fig. 2).

2. DATA

The IGA consists of 60 and 100 μm high spatial resolution images of the Galactic plane plus the Taurus, Ophiuchus, and Orion star molecular clouds (Cao et al. 1997). Briefly, the IGA images were processed using HIRES, a variation of the Richardson-Lucy resolution enhancement algorithm that is flux-conserving and optimized for use with *IRAS* data.

The spatial resolution varies with wavelength; see Table 1 for values. In the analysis presented here we take the ratio of the 60 and 100 μm intensity images, the first step of which is to match the images to a common spatial resolution. For ratio maps we performed additional processing of the IGA images using the HIRES beam-matching technique, which reproduces the complicated *IRAS* beam with high fidelity (Fowler & Aumann 1994; Kerton & Martin 2001). This technique uses the 60 μm HIRES image as a (high-resolution) model of the sky, which is processed to make a (lower resolution) 100 μm image using the actual *IRAS* scan pattern and detector profiles.

Before computing the ratio image, the background emission from cold (∼20 K) cirrus emission associated with H I clouds is subtracted from both the 60 and 100 μm images. The background model multiplies the integrated H I brightness temperature image by an H I–to-FIR conversion constant. The adopted conversion constant was derived by Terebey & Fich (1986) for the infrared cirrus in a nearby ($l = 125°$) field. The background model has little spatial structure and is constant to within 10% over the field of

TABLE 1
SURVEY SPATIAL RESOLUTION

Wavelength	Description	$\theta_{\rm maj}$[a] (arcsec)	$\theta_{\rm min}$[a] (arcsec)	P.A. (deg)
60 μm	IGA[b]	105	50	30
100 μm	IGA[b]	162	113	24
21 cm	DRAO[c]	75	67	158
73 cm	DRAO[c]	205	184	150

NOTE.—Spatial resolution is measured from images. To compare images with different spatial resolutions, the images were beam-matched. The *IRAS* images used the HIRES beam-matching technique described by Fowler & Aumann 1994. For other images, the highest spatial resolution image was convolved with an elliptical Gaussian kernel.

[a] FWHM of two-dimensional elliptical Gaussian fit. P.A. is measured counterclockwise from the vertical axis.

[b] Cao et al. 1997.

[c] Normandeau et al. 1997.

interest, having a value of 10.6 ± 1.0 MJy sr^{-1} at 60 μm. The *IRAS* intensity ratio is then color-corrected (Beichman et al. 1988), for example, changing the median 60 μm/100 μm intensity ratio across the W4 shell from the observed value, 0.51, to the corrected value, 0.55, for $\beta = 1$ dust opacity. The corresponding change in temperature is from 35.0 K to the 36.6 K color-corrected value.

The radio continuum images (Table 1 and Fig. 1) of the W3-W4-W5 region are derived from the DRAO Pilot Survey, the initial product release of the DRAO Canadian Galactic Plane Survey (CGPS; Normandeau et al. 1997). The CGPS consists of radio continuum images at 1420 and 408 MHz, as well as 1420 MHz (21 cm) H I line images. The background due to nonthermal emission was estimated as the median brightness temperature value near the top of W4 (in Fig. 6, a 50′ strip at the top of the image). The background brightness temperature is 1.61 K at 21 cm and 57.7 K at 73 cm, with an estimated 10% 1 σ uncertainty. The computed background spectral index of -2.9 is consistent with that expected for nonthermal emission.

3. THE STRUCTURE OF THE W4 LOOP

3.1. *Luminosity*

In this section, we show that dust plays a small role in absorbing starlight from the OCl 352 cluster. The infrared emission from H II regions is composed of thermal emission from dust, which absorbs and reprocesses shorter wavelength stellar photons. Early studies of the H II region spectral energy distributions (SEDs), made using the Kuiper Airborne Observatory, showed that the flux density measured in janskys typically peaks at 100 μm (Harvey, Campbell, & Hoffmann 1977; Lester et al. 1985). We find that the SED of W4 also peaks at 100 μm, based on the *COBE* DIRBE data (Boggess et al. 1992). The SED was constructed from the large (0.°7) DIRBE beam data over the 10 photometric bands covering 1–240 μm using the on-line DIRBE Small Source SED browser.[6]

Because of *IRAS*'s higher spatial resolution we use the *IRAS* 60 and 100 μm fluxes to compute the total infrared luminosity. Since the SED peaks near 100 μm, this procedure gives infrared luminosities accurate to about 30%, as discussed by several authors (Helou et al. 1998; Leisawitz & Hauser 1988). Total flux is measured using a 50 pc (1.°3) diameter aperture centered on the W4 loop, which includes several bright emission regions. This is the same aperture used later (§ 3.5) for the thick-shell model. The images have been corrected for the infrared background associated with H I, but there was no additional subtraction of a local background. This was done to ensure that we obtained an upper limit to the infrared flux from the W4 loop, although it means that the flux, and therefore luminosity, includes contributions from W3 and other neighboring regions.

The flux density of W4 is 27,000 Jy at 60 μm and 54,000 Jy at 100 μm, which, following Leisawitz & Hauser (1988), implies a total infrared luminosity $L_{\rm IR} = 3.0 \times 10^5\ L_\odot$ at the 2.2 kpc distance of W4. The total luminosity emitted by cluster stars is $L_{\rm OB} = 4.3 \times 10^6\ L_\odot$, of which $L_{\rm ion} = 2.2 \times 10^6\ L_\odot$ is contributed by ionizing photons, where the values are derived using the O star content (Humphreys 1978; Normandeau et al. 1996), model luminosities (Schaerer & de Koter 1997), and fractional energy of the ionizing photons (Panagia 1973). Dust absorption from both ionizing and nonionizing photons contributes to the infrared luminosity. Assuming that the dust absorbs only ionizing photons implies that the dust absorbs less than 14% of the energy produced by the ionizing photons, computed by construction as a conservative upper limit. This implies that absorption by dust does not play a significant role in the transport of ionizing photons in the H II region. Leisawitz & Hauser (1988) and Leisawitz (1991) find a similar result for several other Galactic H II regions.

[6] See http://nssdc.gsfc.nasa.gov/ir/cobe/dirbe/spect.html.

3.2. *Global Ionization*

We now assess what fraction of ionizing photons from the massive star cluster are absorbed by the W4 H II region/superbubble. We neglect dust absorption (see § 3.1) and nonthermal radio emission (see § 3.3) as unimportant. We first estimate the total radio continuum flux that is produced by ionizing photons from the star cluster. The global balance between the rates of ionization and recombination in an H II region is given by $N_{\rm ion} T = \alpha_B n_e^2 V$, where $N_{\rm ion}$ is the number of ionizing photons per second emitted by the star cluster, T the fraction of ionizing photons that are absorbed ($T = 1$ for ionization bounded), $\alpha_B = 2.58 \times 10^{-13}$ cm^3 s^{-1} the recombination rate coefficient for hydrogen at 10,000 K, and V the ionized gas volume. To evaluate the shell model, whose center is offset from the star cluster, we use the generalized expression $N_{\rm ion} T d\Omega/4\pi = \alpha_B n_e^2 dV$, where $d\Omega/4\pi$ is the solid angle from the ionizing source to dV, the volume element (Miller & Cox 1993). The volume emission measure is in turn related to the observed radio continuum flux S_ν by $S_\nu D^2 = j n_e^2 dV$, where $j = 3.13 \times 10^{-40}$ ergs cm^3 s^{-1} sr^{-1} Hz^{-1} is the 21 cm free-free emissivity. For flux $S_{\rm Jy}$ expressed in janskys, then, $n_e^2 dV = 1.40 \times 10^{60} S_{\rm Jy}$ at a 2.2 kpc distance. The rate of cluster ionizing photons is $Q = 2.3 \times 10^{50}$ s^{-1}, estimated from the O star content (Dennison et al. 1997). In the case of an ionization-bounded H II region ($T = 1$), combining the above expressions leads to a prediction of 640 Jy for the total radio continuum flux at 21 cm that arises from the OCl 352 cluster.

There is a small (12′ diameter) clump of continuum emission near the star cluster. The 21 cm flux of the clump is 9.0 Jy, which, assuming a 4π emitted solid angle, implies that less than 2% of the cluster ionizing photons are absorbed by the clump. The radio continuum clump corresponds to the location denoted "SC" by Dennison et al. (1997). Using Hα measurements, they infer that 7% of the cluster ionizing photons are absorbed by the clump. The reason for the disagreement is not clear but is likely to be related to the large extinction correction that has been applied to the Hα data. Both results imply that the sphere of influence of the ionizing stars is much larger than the clump. Next we consider the radio flux over a larger aperture that contains the W4 loop. The radio continuum flux of 116 Jy, measured within a 50 pc (1.°3) diameter aperture, implies that 18% of the total ionizing photons are absorbed in the vicinity of the W4 loop.

The remaining ionizing photons appear to be able to escape the W4 loop. Direct evidence is given by a halo of radio continuum emission (see § 3.7) surrounding W4. The low observed infrared luminosity (see § 3.1) argues that absorption of ionizing photons by dust is unimportant and can be neglected.

The massive star cluster OCl 352 is likely to be the main source of ionization (Normandeau et al. 1996). The image (Fig. 2) also shows a lesser known H II region associated with an embedded star cluster near BIRS 101 to the upper right at $l = 134.^{\circ}3$, $b = 0.^{\circ}8$ (Elmegreen 1980). The stellar content is unknown, but we argue that this region is not likely to contribute more ionizing photons than OCl 352. Consider that the radio flux is proportional to the ionizing photon flux through the recombination balance equation. This means that the embedded cluster contains stars that are no more massive than those in the OCl 352 cluster, given that the two clusters have equal 21 cm flux measured with the same 12′ aperture. In fact, it likely has *lower* intrinsic ionizing flux, because the higher gas density and extinction around the embedded cluster implied by the stronger IR emission mean that more photons will be captured locally.

3.3. *Radio versus Infrared Comparison*

The focus of our modeling effort is the W4 loop, displayed in Figure 2 with the positions of the three most massive O stars (O4–O5) in OCl 352 marked. Most of the emission in the 60 μm image traces column density rather than temperature (see § 3.4). The correspondence seen between the 60 μm and 21 cm continuum images is indirect, as the FIR emission is sensitive to warm (20–60 K) dust, whereas the 21 cm continuum traces ionized gas. There is an overall correlation with slope $m = I_{60\mu\mathrm{m}}/I_{21\mathrm{cm}} = 230$ with significant scatter. To understand the source of the "scatter," we map the outlying points back into image space, to look for geometrically distinct regions. We adopt the excess map technique of Gaustad & Van Buren (1993) and form a difference image, $I_{21\mathrm{cm}} - I_{60\mu\mathrm{m}}/m$, which serves to eliminate structure common to both images.

The remarkable difference image (Fig. 2, *middle panel*) reveals striking spatial differences between ionized gas and warm dust. The loop structure displays enhanced 21 cm emission (*white*) lying interior to the enhanced 60 μm emission (*black*). Complete ionization in the H II region is a good assumption, which implies that the 21 cm intensity $I_{21\mathrm{cm}}$ is proportional to the emission measure expressed as $n_e^2 L_i$, where L_i is the ionized gas path length. The enhanced continuum emission seen on the inner edge traces high ionization and suggests that the loop is ionization-bounded, meaning that the shell's interior is ionized but the exterior is neutral. In § 3.6, we return to the apparent contradiction of an ionization-bounded shell where most of the ionizing photons escape.

The FIR emission is generally accepted to be thermal emission from dust that is efficiently heated by the UV component of the local interstellar radiation field (Terebey & Fich 1986; Boulanger et al. 1988). The enhanced FIR emission at the outer loop edge appears to be due to nonionizing UV photons from the OB cluster that travel into the compressed shell, where the dust optical depth is significant (Leisawitz & Hauser 1988). The infrared data (see § 3.4) show a corresponding gradient in the dust temperature across the shell.

The spectral index of the radio continuum emission was derived from the ratio of the beam-matched (and background-subtracted) 21 and 73 cm images. Over the W4 loop region the median flux density spectral index is 0.08, which is approximately consistent with the -0.1 expected for free-free emission from optically thin ionized gas at a constant temperature. This confirms that the continuum emission seen in the 21 cm image is primarily due to ionized gas.

3.4. *Dust Temperature and Optical Depth from Infrared Data*

The intensity due to thermal dust emission is, for optically thin emission, given by $I = B_\nu(T_D)\tau$, where B_ν is the Planck function, T_D is the dust temperature, and the dust optical depth is $\tau = \kappa\rho L$, where κ is the dust opacity, assuming a standard dust-to-gas ratio, ρ is the gas density, and L is the line-of-sight path length. We express the dust opacity as $\kappa = 0.1\ \mathrm{cm^2\ g^{-1}} (250\ \mu\mathrm{m}/\lambda_{\mu\mathrm{m}})^{\beta}$ (Hildebrand 1983), where $\lambda_{\mu\mathrm{m}}$ is the wavelength in microns and $\beta = 0$–2 is a standard range. We adopt $\beta = 1$ for FIR wavelengths; an uncertainty of $\beta = \pm 0.5$ translates into a systematic uncertainty in the temperature scale of ∓ 4 K. The FIR emission is often associated with neutral ISM gas, but since the dust is not well coupled to the gas at the expected densities, $n \lesssim 5\ \mathrm{cm^{-3}}$, we assume that the dust emissivity is unchanged in the ionized shell. For a constant dust temperature the 60 μm intensity is then proportional to the total—neutral plus ionized—gas column through the shell. The dust "color" temperature T_c is derived from the 60 μm/100 μm intensity ratio, where the 60 μm data are beam-matched to the 100 μm resolution. For a nonuniform medium the dust color temperature is weighted toward the warmest dust along the line of sight.

Figure 3 shows the derived 100 μm optical depth and dust color temperature images. The W4 loop is seen clearly in the optical depth map. The shell appears patchy, with low column density regions visible toward the shell's left-hand edge and geometric center (below the cluster stars). There is cold, high column density material visible below the bottom edge of the W4 loop; the FIR data thus provide direct evidence of the dense ISM needed to stall the superbubble's expansion at its base.

The color temperature image (Fig. 3, *right-hand panel*) shows a dust hot spot coincident with one of the cluster ionizing stars. There is also what appears to be a large bubble of warm dust associated with W4. On the right and at the lower boundary of the bubble, the warm dust coincides with the inner edge of W4 loop and exhibits a significant temperature drop across the shell, as might be expected for an ionization-bounded shell. However, to the left the warm dust extends well past the W4 loop boundary. The shell column density is also very low on the left, which suggests that the shell is not ionization-bounded on the left-hand side.

The bubble of warm dust has a nearly constant temperature, $T = 37 \pm 1.8$ K, with a distinct boundary seen along its lower edge, where the dust temperature drops quickly by 3–4 K. Below the boundary the temperature drops monotonically, falling to 15–20 K along the image's bottom edge. The explanation for the nearly constant temperature of the bubble is unclear. It is possible that the warm dust is radiatively heated and thus defines the ionization boundary of the H II region. Arguing against this, the radio image shows ionized gas exterior to this region (see § 3.7). Alternatively, if the warm dust is collisionally heated it may trace dust within the hot (10^6 K) superbubble interior. More theoretical modeling would be useful to determine the source of the dust heating.

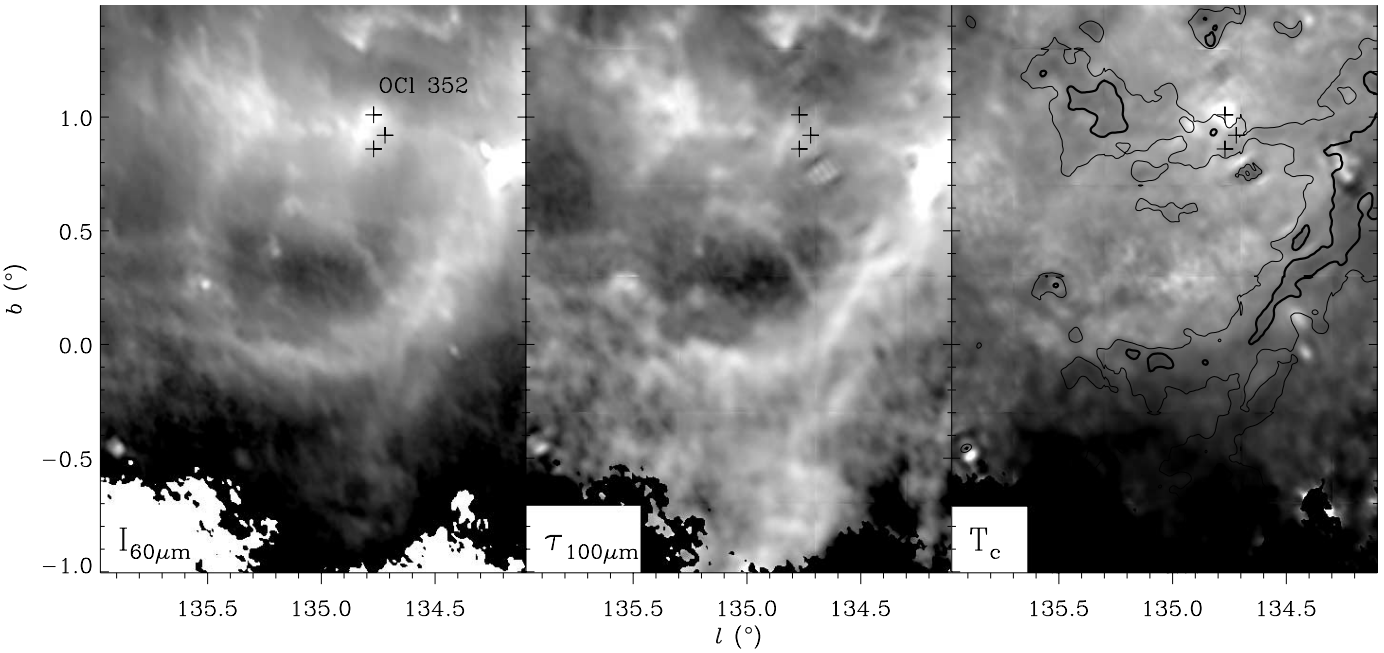

FIG. 3.—Optical depth and temperature across the W4 loop. *Left*: Background-subtracted 60 μm intensity image. As the other panels demonstrate, most of the structure represents column density rather than temperature variation. The data confirm that the OCl 352 OB cluster is the source of ionization and heating. The display uses 0.5 MJy sr^{-1} < log I_{60} < 2.5 MJy sr^{-1}. The τ_{100} optical depth map (*middle*) reveals dense, relatively cool material below ($b < 0°$) the limb-brightened shell. This dense material is predicted by the W4 chimney model to explain why blowout occurs above rather than below the powering OCl 352 cluster. The shell is inhomogenous; low column density extends from the lower middle (135.°0, 0.°2) to the left. The display uses $-5.0 < \log \tau_{100} < -3.0$. Low-intensity regions ($I_{60} < 0.5$ MJy sr^{-1} in the background-subtracted map) are masked out to minimize unreliable structure due to noise in the ratio map (*middle and right-hand panels*). *Right*: Dust color temperature derived from the I_{60}/I_{100} intensity ratio. Overplotted are $\tau_{100} = 0.0002$ (*thin*) and 0.0005 (*thick*) optical depth contours. The hot spot near one OCl 352 cluster member indicates locally heated dust. Across much of the W4 superbubble the dust temperature is nearly constant at 36 K; to the left the warm dust extends far past the barely visible shell edge. The shell is much thicker to the lower right; there is a corresponding abrupt temperature decrease at the shell's inner edge. The display uses 25 K < T_c < 45 K.

3.5. *Shell Models*

The loop morphology of W4 suggests a limb-brightened shell. Figures 4 and 5 compare the infrared and radio data with two shell models that bracket the plausible range of fits. Dennison et al. (1997) present a shell model for their Hα data that is consistent with our best fit for the radio continuum. The spatial structure in the optical depth map implies that there are large density variations across the W4 loop. Nevertheless, the loop structure is sufficiently regular to attempt fitting a shell model. The spherical assumption is admittedly simplistic, as the OCl 352 powering star cluster lies at the top edge, rather than the geometric center, of the model. If the shell has radius R and thickness δR, then the maximum contrast ratio between shell edge and shell center is given by $(2R/\delta R - 1)^{0.5}$; a spatial resolution that is comparable to or larger than the shell thickness will reduce the observed contrast ratio. For completeness we also describe the ring model, i.e., a torus of material. The main distinguishing feature is that the ring model predicts no emission inside the ring in a two-dimensional projected image. The data appear inconsistent with the ring model.

Figure 4 shows the infrared model comparison, and Table 2 gives shell model parameters. The thin-shell model has one-quarter the thickness of the thick-shell model and exhibits correspondingly stronger limb brightening. The data show strong density inhomogeneities on a large scale, but generally lie within a factor of 3 of the model value. The

TABLE 2
PARAMETERS OF W4 DUST SHELL MODEL

Model	l_{cen}[a] (deg)	b_{cen}[a] (deg)	δR[b] (arcmin)	R_{in}[c] (arcmin)	δR[b] (pc)	R_{in}[c] (pc)	τ_{cen}[d]	n_H[e] (cm^{-3})	M_{sh} ($M_\odot$)
Thick	135.02	0.42	10	30	6.4	19	0.00011	4.8	6700
Thin	135.02	0.42	2.5	30	1.6	19	0.00011	19	5300

NOTE.—Assumes $D = 2.2$ kpc, $\kappa = 0.25$ cm^2 g^{-1} at 100 μm, mean mass per $H = 1.4$.
[a] Position of model shell center in Galactic coordinates.
[b] Shell thickness.
[c] Inner radius of shell.
[d] Model 100 μm optical depth at center position; includes front and back of shell.
[e] Gas density in model shell. Assumes standard dust-to-gas ratio.

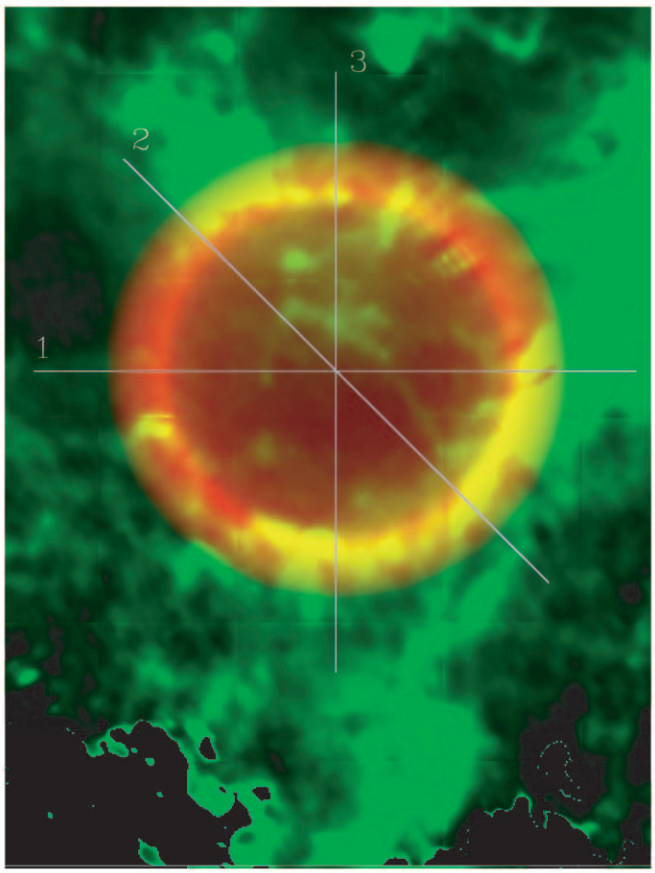

FIG. 4*a*

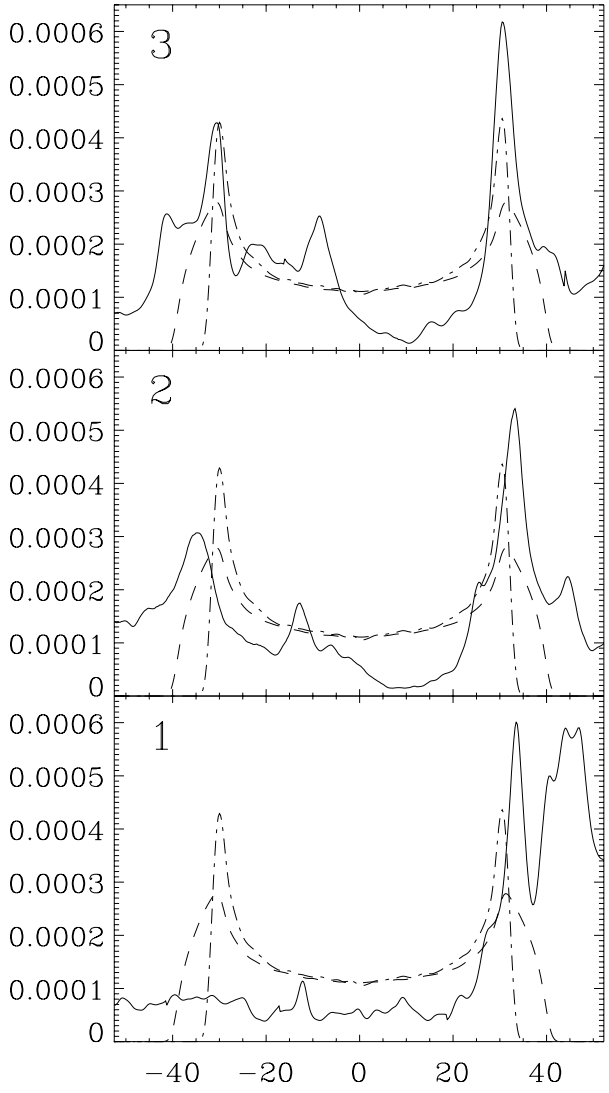

FIG. 4*b*

FIG. 4.—(*a*) W4 thick-shell model (*red*) superposed on the optical depth map (*green*) of the dust at 100 μm. The numbered lines indicate the positions of slices plotted in (*b*). (*b*) Optical depth vs. distance from the nominal shell center. Data (*solid line*) and two models from Table 2 are shown. Models have been convolved with the 100 μm beam. Deviations from sphericity favor the thick-shell model, while the sharp horns of the line profiles favor the thin-shell model. The shell is patchy, but appears consistent with an inhomogenous shell rather than a thin ring, i.e., torus.

density is higher than average on the right-hand and lower quadrants of the shell, while the very faint shell signature at the center and left-hand edge suggests that the hot superbubble gas may have "broken out" in these areas. Overall, the thick-shell model seems to fit the data better; however, the thin-shell model fits the "horns" well, which would imply that the inner edge of W4's shell has about 4 times higher density.

Figure 5 shows the radio continuum model comparison, and Table 3 gives shell model parameters. The deviations

TABLE 3

PARAMETERS OF W4 IONIZED SHELL MODEL

Model	l_{cen} (deg)	b_{cen} (deg)	δR (arcmin)	R_{in} (arcmin)	δR (pc)	R_{in} (pc)	T_B[a] (K)	S_I[b] (Jy)	S_{obs}[c] (Jy)	$n_e^2 2\delta R$[d] (pc cm^{-6})	n_e (cm^{-3})	M_{sh}[e] ($M_\odot$)
Thick	135.02	0.42	10	30	6.4	19	2.07	84	107	1330	10	14400
Thin	135.02	0.42	2.5	30	1.6	19	2.07	66	70	1330	20	5700

NOTE.—Size and thickness of model shell is the same as in Table 2. The factor 6.20×10^4 Jy sr^{-1} K^{-1} converts from brightness temperature to flux.

[a] The 21 cm model brightness temperature at center position; includes front and back of shell.

[b] Total flux of model shell.

[c] Total observed flux that falls inside model-defined aperture. Note that 9.0 Jy of flux contributed by the compact OCl 352 H II region has been subtracted.

[d] Emission measure at center position, derived from model brightness temperature and assuming 10,000 K temperature and optically thin gas.

[e] Mass assumes completely ionized gas.

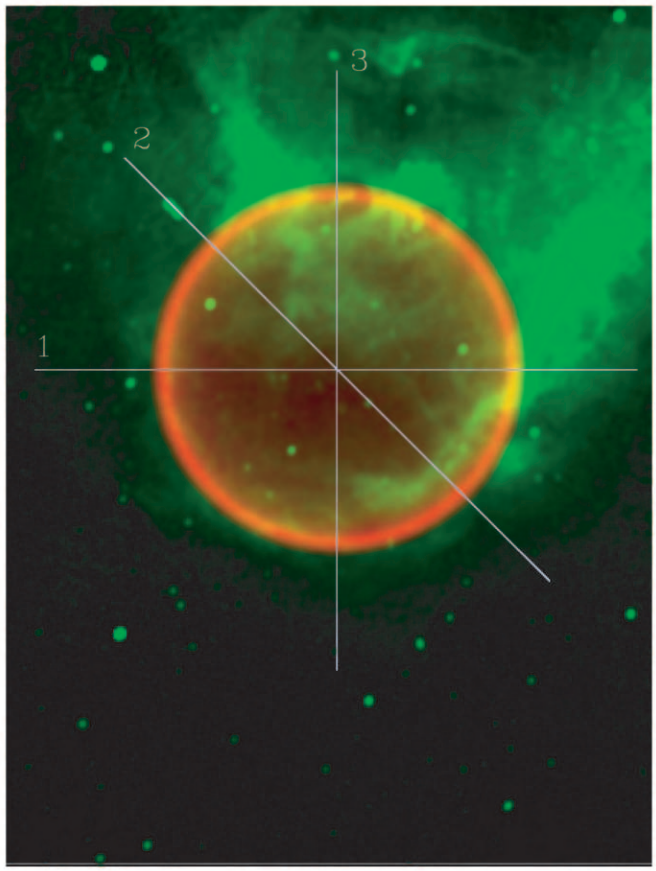

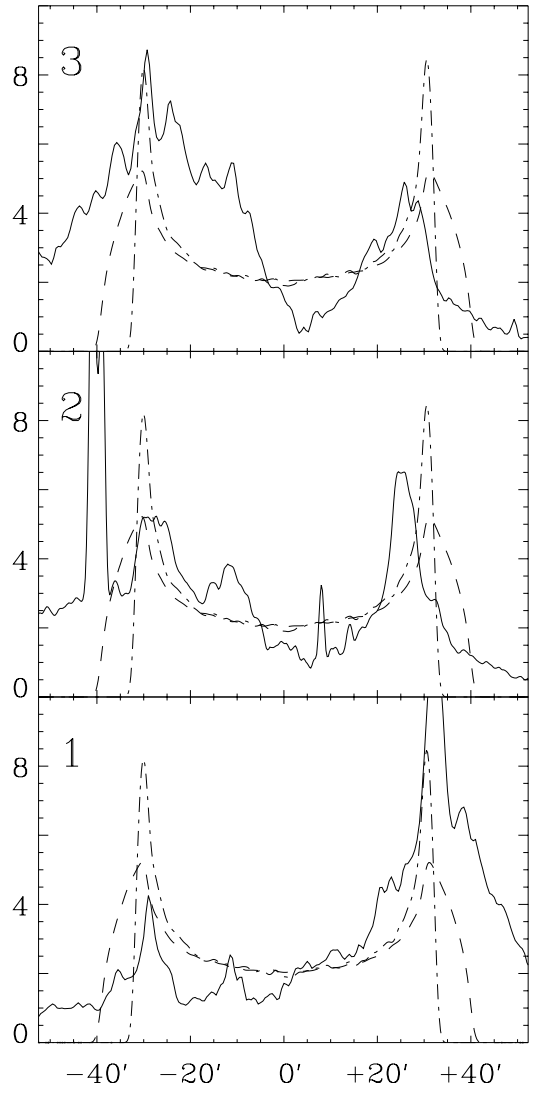

FIG. 5*a* FIG. 5*b*

FIG. 5.—(*a*) W4 thin-shell model (*red*) superposed on the 21 cm radio image (*green*) of the ionized gas. The numbered lines indicate the positions of slices plotted in (*b*). (*b*) Profiles of observed and predicted radio emission vs. distance from the nominal shell center. Data (*solid line*) and two models from Table 2 are shown. Models have been convolved with the 21 cm beam. The sharp horns of the line profiles favor the thin-shell model. The ionized shell is patchy, but appears consistent with a shell rather than a thin ring, i.e., torus. Fig. 2 shows that the ionized gas lies interior to the dust emission, suggesting that the shell is ionization-bounded.

from the shell model are smaller, roughly a factor of 2, and the thin-shell model provides a better fit. The positions of the model peaks are unchanged, so that the infrared and radio profiles in Figures 4*b* and 5*b* can be compared directly. In profile 2, the radio horns clearly lie interior to the infrared horns, confirming the offset seen in Figure 2.

The inferred mass suggests that the shell represents swept-up ambient material. Mass loss from the stars contributes little to the total; assuming a mass-loss rate of 1×10^{-5} $M_{\odot}$ yr^{-1} and cluster age of 3.7–5.7 Myr (Normandeau et al. 1996) leads to a 37–57 $M_{\odot}$ stellar wind mass, which is tiny compared with the infrared-derived shell mass. If the shell represents swept-up ambient ISM, then the inferred ambient density is 2.8–4.0 cm^{-3}, which compares favorably with the 5 cm^{-3} estimated for the H I by Normandeau et al. (1996).

Above, we assumed that the dust-to-gas ratio was constant in the neutral and ionized shell. The FIR data suggest a shell mass of 5300–6700 $M_{\odot}$ (Table 2), which should include both the neutral and ionized gas mass. At first, this seems inconsistent with the 5700 $M_{\odot}$ found for the ionized thin-shell model. However, the ionized value represents an upper limit, because we assumed a filling factor $f = 1$, but the ionized mass scales as $f^{0.5}$ for a given volume emission measure. We conclude that the infrared and radio shell models are consistent but that the infrared data provide a more reliable estimate of the total shell mass.

3.6. *Ionization Trapping Factor*

We now investigate whether some parts of the shell are ionization-bounded by evaluating the trapping factor T (§ 3.2) for various parts of the shell. In § 3.2, we found that 18% of total ionizing photons are absorbed in the vicinity of the W4 loop. Because the star cluster lies along the top edge of the model shell, we further partition the ionizing photons by $N_{\rm ion} = Q/2$, which represents the photons that are directed downward and can be intercepted by the shell. Over

the aperture defined by the thin-shell model, the observed flux of 70 Jy leads to $T = 0.22$ trapping factor. The trapping factor is larger for the most distant parts of the shell. For example, the bottom half of the shell subtends a solid angle $0.29 \times 2\pi$, which implies $T = 0.71$. For the most distant part of the shell $T = 0.80$, using model emission measure $n_e^2 \delta R = 664$ at $2R = 38$ pc distance. In § 3.5, we showed that the shell was inhomogeneous, with factor of 2–3 density variations. Therefore, overdense regions in the bottom half of the shell will easily trap all of the ionizing photons. This explains why a large fraction of the shell can appear ionization-bounded, even though a modest fraction of the total ionizing photons are locally absorbed.

Our results differ from the Hα results of Dennison et al. (1997), who argue that few ionizing photons escape the W4 superbubble. Below the star cluster they fit a similar thin-shell model to the W4 loop, but conclude that it is ionization-bounded; we ascribe the difference to the large and uncertain extinction correction, which does not affect the 21 cm emission but must be applied to the Hα flux. They see little Hα flux in the W4 chimney above the star cluster. There is a cometary-shaped molecular cloud (Heyer et al. 1996; Taylor et al. 1999) just above the cluster, which they argue is blocking the ionizing radiation from traveling up the W4 chimney. However, this cometary cloud should reemit copious emission at either radio or FIR wavelengths, sufficient to explain trapping half the cluster ionizing flux. However, our data show only modest emission from the cometary cloud region (to the right of the numeral 3 in Figs. 4 and 5), containing much less total flux than is seen from the W4 loop. We conclude that most of the upward-directed ionizing photons escape freely and can travel large distances up the W4 chimney.

3.7. *Halo of Ionized Gas Outside the W4 Shell*

We previously showed that 18% of the ionizing photons from the massive star cluster are absorbed in the W4 loop; consider now what happens to the ionizing photons that escape. The total required 21 cm flux is 640 Jy for W4 to be ionization-bounded ($T = 1$). However, integrating the flux over successively larger regions, we find that it approaches but never reaches this value. We estimate a $1\ \sigma = 0.16$ K uncertainty in the background level, which corresponds to a 100 cm^{-6} pc uncertainty in the emission measure. In § 3.2, we found that 116 Jy flux was observed near the W4 loop. The total flux measured over the entire W4 loop image (Fig. 5) is 210 ± 28 ($2\ \sigma$) Jy, which says that 33% of the total ionizing photons are absorbed on that scale. Note that no correction is made to exclude point sources, which therefore contribute a small amount of unwanted flux to the total.

Examining W4 on a larger scale, we find that the radio continuum data in Figure 6 display a faint halo of ionized gas surrounding W4 (Gray et al. 1999). The halo extends outside the W4 loop, demonstrating that even though the shell is substantially ionization-bounded, it is patchy and lets ionizing photons escape. Excluding the region around W3 (*white rectangle*), then, the total flux over the entire Figure 6 image is 380 ± 104 ($2\ \sigma$) Jy. This flux is an upper limit to the flux from W4, as it includes contributions from unrelated ionizing sources (W3) and unrelated point sources. We conclude that $40\% \pm 16\%$ ($2\ \sigma$) of the ionizing photons escape ($>1\overset{\circ}{.}5 = 60$ pc) the W4 chimney/superbubble. These photons travel preferentially along the low-density W4 chimney and are available to ionize the DIG and upper Galactic halo.

The maximum distance to which ionizing photons can travel is difficult to assess from these data because of the uncertainty in the background determination. However, the data are consistent with very low density in the chimney region above the star cluster. Note that the Perseus arm, where W4 resides, is the main area of star formation and molecular clouds in the outer Galaxy, so that the density is expected to decrease away from the spiral arm (Heyer & Terebey 1998). In addition, the W4 chimney model calls for a decreasing density gradient above the Galactic plane, which the data seem to confirm; below the star cluster the radio continuum is about 2 K (see W4 shell model), whereas the emission drops to zero about $1\overset{\circ}{.}0 = 40$ pc above the cluster ($b = 2°$) in the chimney region. The FIR optical depth map implies a similar gradient in column density; the dense material below the W4 loop at $b = -0\overset{\circ}{.}3$ has a median optical depth of about 1.6×10^{-4}, while the column density declines by a factor of 5, to about 3.0×10^{-5}, at $b = 2\overset{\circ}{.}2$, above and roughly equidistant from the star cluster.

4. SUMMARY

We have shown that there is a strong correspondence between the FIR and radio continuum in the IGA and DRAO 21 cm Galactic plane surveys (Fig. 1). The emission is due to thermal processes (dust and ionized gas). Analysis of a subregion centered on the lower W4 loop supports the Normandeau et al. (1996) W4 chimney hypothesis, in which a swept-up shell is powered by the OCl 352 OB cluster.

1. The lower W4 loop exhibits shell structure at both FIR and radio wavelengths. We construct a difference map to study spatial differences and find that the ionized gas lies interior to the dust. The morphology suggests an ionization-bounded shell.

2. We construct dust temperature and optical depth maps from the FIR data. The 100 μm optical depth map shows direct evidence of dense material (median $\tau_{100} = 1.6 \times 10^{-4}$) at the bottom of the W4 shell that appears to have retarded shell expansion in this direction. The dust optical depth also shows evidence for the steep density gradient proposed for the chimney model; in the chimney region, located roughly equidistant above the star cluster, the optical depth is 5 times lower than that found at the base of the superbubble.

3. There is a bubble of warm ($T = 37$ K), nearly constant temperature dust associated with W4. The warm dust coincides with the inner edge of the W4 loop, as might be expected for an ionization-bounded shell. However, the warm dust extends past the W4 loop boundary on the left-hand edge. If the warm dust is associated with the hot superbubble interior, then its appearance suggests that the bubble has achieved blowout on the left-hand edge, where the shell column density is lowest. Theoretical modeling of the dust temperature expected from superbubble interiors would be useful to determine the warm dust origin.

4. Fits to the lower W4 loop in both the FIR and radio continuum data reveal a thin shell, which extends 40 pc below the cluster. The derived shell mass is about 5300–6700 $M_\odot$, with density of 4.8 cm^{-3}, implying 2.8–4.0 cm^{-3} for the ambient density. The inner edge of the shell has a higher density of 20 cm^{-3} and appears to be ionized, rather than neutral, gas. The shell is very inhomogeneous, showing

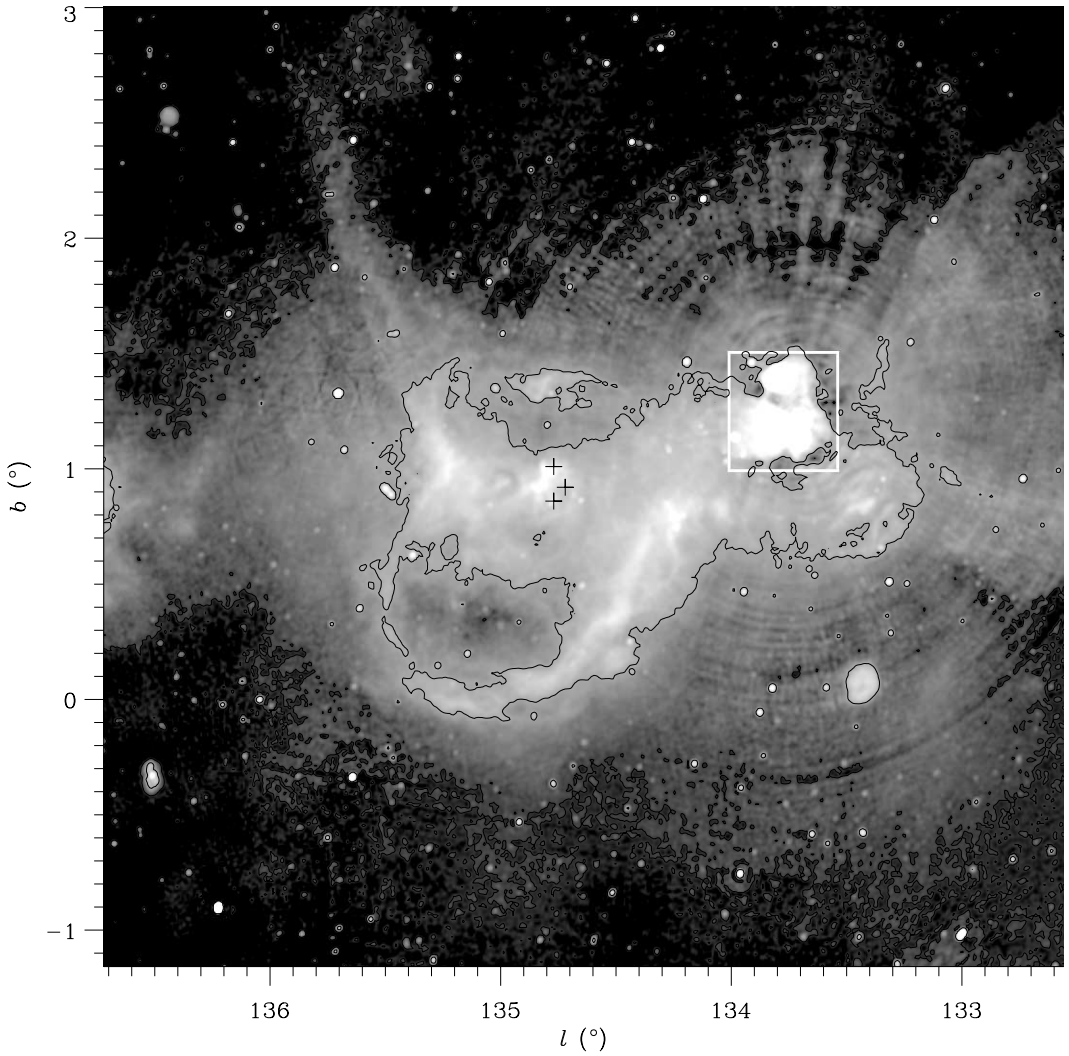

FIG. 6.—The log stretch of the background-subtracted 21 cm image, showing the faint, diffuse, ionized halo surrounding W4. Three crosses mark the brightest O stars in the OCl 352 cluster. Two contour levels are displayed, at 2 and 20 σ, where $\sigma = 0.16$ K is the uncertainty in the background determination. The $\sim 3^\circ = 120$ pc halo is reliably detected down to the 2 σ contour level, which corresponds roughly to the faintest emission visible in this stretch. The low-density ionized halo is approximately centered on the star cluster, but extends well outside the W4 loop (20 σ contour). This demonstrates that the inhomogeneous shell lets ionizing photons escape, even though large parts of the W4 shell are ionization-bounded. The white rectangle outlines the neighboring W3 H II region. The log I_{21} intensity stretch has a [−1, 1.25] range.

factors of 2–3 variation in density. The observed FIR luminosity of 3.0×10^5 $L_\odot$ represents 7% of the total cluster luminosity.

5. To approximate the nonspherical structure of the lower W4 loop, we model the ionizing cluster as lying on the top edge of a spherical shell. The trapping efficiency of the shell to ionizing photons thus varies with distance from the cluster. The entire shell traps 22% of the available (downward-directed) photons, whereas the bottom half of the shell traps 71% of the available ionizing photons. The factor of 2–3 density variation suggests that the overdense parts of the shell will easily trap all the photons and therefore explains why the shell can appear ionization-bounded even though a modest fraction of the total ionizing photons are absorbed.

6. The lower shell absorbs roughly 18% of the cluster ionizing photons. Over a larger region centered on W4, the fraction rises to roughly 33% of the ionizing photons. Examination of the radio continuum image at low levels shows a faint, ionized halo surrounding W4. The halo extends past the shell boundary, further evidence that the patchy shell can let ionizing photons escape. After integrating the ionized flux over the largest plausible aperture, we find that $40\% \pm 16\%$ (2 σ) of the ionizing photons escape (>60 pc) the W4 chimney/superbubble. These photons travel preferentially along the low-density W4 chimney and are available to ionize the DIG and upper Galactic halo. This case study of the W4 chimney supports recent proposals that O stars provide the ionizing photons that are needed to produce the extended DIG observed in external galaxies (Dove & Shull 1994; Ferguson et al. 1996; Oey & Kennicutt 1997).

S. Terebey thanks D. Van Buren for useful discussions and thanks NASA for support from the Astrophysics Data Program contract NAS 5-97066.

REFERENCES

Basu, S., Johnstone, D., & Martin, P. G. 1999, ApJ, 516, 843
Beichman, C. A., et al., ed. 1988, *IRAS* Catalogs and Atlases: Explanatory Supplement (NASA RP-1190; Washington: GPO)
Boggess, N. W., et al. 1992, ApJ, 397, 420
Boulanger, F., Beichman, C. A., Désert, F. X., Helou, G., Pérault, M., & Ryter, C. 1988, ApJ, 332, 328
Braunsfurth, E., & Feitzinger, J. V. 1983, A&A, 127, 113
Cao, Y., Terebey, S., Prince, T. A., & Beichman, C. A. 1997, ApJS, 111, 387
Carpenter, J. M., Heyer, M. H., & Snell, R. L. 2000, ApJS, 130, 381
Cox, D. P. 1989, in IAU Colloq. 120, Structure and Dynamics of the Interstellar Medium, ed. G. Tenorio-Tagle, M. Moles, & J. Melnick (LNP 350; Berlin: Springer), 500
Dennison, B., Topasna, G. A., & Simonetti, J. H. 1997, ApJ, 474, L31
Dove, J. B., & Shull, J. M. 1994, ApJ, 430, 222
Elmegreen, D. M. 1980, ApJ, 240, 846
Ferguson, A. M. N., Wyse, R. F. G., Gallagher, J. S., III, & Hunter, D. A. 1996, AJ, 111, 2265
Fowler, J., & Aumann, H. H. 1994, in Science with High Spatial Resolution Far-Infrared Data, ed. S. Terebey & J. M. Mazzarella (Pasadena: JPL), 1
Fürst, E., Reich, W., & Sofue, Y. 1987, A&AS, 71, 63
Gaustad, J. E., & Van Buren, D. 1993, PASP, 105, 1127
Gray, A. D., Landecker, T. L., Dewdney, P. E., Taylor, A. R., Willis, A. G., & Normandeau, M. 1999, ApJ, 514, 221
Harvey, P. M., Campbell, M. F., & Hoffmann, W. F. 1977, ApJ, 211, 786
Haslam, C. G. T., & Osborne, L. L. 1987, Nature, 327, 211
Helou, G., Khan, I. R., Malek, L., & Boehmer, L. 1988, ApJS, 68, 151
Heyer, M. H., Brunt, C., Snell, R. L., Howe, J., Schloerb, F. P., & Carpenter, J. H. 1998, ApJS, 115, 241
Heyer, M. H., & Terebey, S. 1998, ApJ, 502, 265
Heyer, M. H., et al. 1996, ApJ, 464, L175
Hildebrand, R. H. 1983, QJRAS, 24, 267
Humphreys, R. M. 1978, ApJS, 38, 309
Kerton, C. R., & Martin, P. G. 2001, PASP, 113, 872
Kulkarni, S., & Heiles, C. 1987, in Interstellar Processes, ed. D. J. Hollenbach & H. A. Thronson, Jr. (Dordrecht: Reidel), 87
Leisawitz, D. 1991, ApJS, 77, 451
Leisawitz, D., & Hauser, M. G. 1988, ApJ, 332, 954
Lester, D. F., Dinerstein, H. L., Werner, M. W., Harvey, P. M., Evans, N. J., II, & Brown, R. L. 1985, ApJ, 296, 565
Mac Low, M.-M., McCray, R., & Norman, M. L. 1989, ApJ, 337, 141
Massey, P., Johnson, K. E., & DeGioia-Eastwood, K. 1995, ApJ, 454, 151
Miller, W. W., III, & Cox, D. P. 1993, ApJ, 417, 579
Normandeau, M., Taylor, A. R., & Dewdney, P. E. 1996, Nature, 380, 687
———. 1997, ApJS, 108, 279
Oey, M. S., & Kennicutt, R. C., Jr. 1997, MNRAS, 291, 827
Panagia, N. 1973, AJ, 78, 929
Reynolds, R. J. 1984, ApJ, 282, 191
———. 1991, ApJ, 372, L17
Reynolds, R. J., Haffner, L. M., & Tufte, S. L. 1999, ApJ, 525, L21
Reynolds, R. J., Sterling, N. C., & Haffner, L. M. 2001, ApJ, 558, L101
Reynolds, R. J., & Tufte, S. L. 1995, ApJ, 439, L17
Schaerer, D., & de Koter, A. 1997, A&A, 322, 598
Shull, J. M. 1996, Nature, 380, 668
Taylor, A. R., Irwin, J. A., Matthews, H. E., & Heyer, M. H. 1999, ApJ, 513, 339
Terebey, S., & Fich, M. 1986, ApJ, 309, L73
Tomisaka, K. 1998, MNRAS, 298, 797
Walterbos, R. A. M., & Braun, R. 1994, ApJ, 431, 156